bioRχiv

New neural-inspired controller generalises modularity over lower limb tasks through internal models

David Muñoz[a,b,*], Dónal Holland[c], and Giacomo Severini[a,b]
[a]School of Electrical and Electronic Engineering, University College Dublin, Dublin, Ireland
[b]Insight Centre for Data Analytics, Dublin, Ireland
[c]School of Mechanical and Material Engineering, University College Dublin, Dublin, Ireland
*Correspondence should be addressed to D.M. (david.munoz@ucdconnect.ie)

Predictive neuromuscular models based on neural controllers are a powerful tool for testing assumptions on the underlying architecture of sensorimotor control and its associated neural activity. However, most current controllers suffer from lack of physiological plausibility and are generally task specific. We propose a new neural controller, called Internal Model-based Modular Controller (IMMC), where a hierarchical architecture organises generalizable modules in activation networks dedicated to different motion tasks. The architecture comprises a simple model of the mesencephalic locomotor region (MLR), which sends controlling signals that manage the activity of internal models (IMs). The IMs organise synergies, coordinated and stereotyped activity of multiple muscles, in task-specific networks. The resultant organisations allow the generalisation of this architecture to different lower limb motions. The IMMC was tested in Stand-To-Walk simulations (STW), where the MLR switches between two IMs that recombine five synergies to replicate the standing and walking tasks. The simulation kinematics, muscle activation patterns and ground reaction forces were generally consistent with experimental data. In addition, the controller can transition to slower and faster speeds by tuning a single controlling signal. The proposed architecture is a first step to develop neuromuscular models which integrate multiple motor behaviours in a unified controller.

Introduction

Predictive neuromuscular models can address gaps in the knowledge of human motor control by testing hypotheses about its inherent neurophysiology (Hicks et al., 2015). Particularly, models that include neural controllers can mimic the role of sensorimotor control in the generation of movements. Current neural controllers present architectures which normally include reflexes, central pattern generators, or a combination of both. These architectures often present challenges related to dimensionality and physiological plausibility.

Dimensionality is the number of parameters that need to be tuned to map a motion. For example, neural controllers that implement reflex loops (Geyer & Herr, 2010; Song & Geyer, 2012, 2015; Muñoz et al., 2022; van der Kruk & Geijtenbeek, 2023), known as reflex-based controllers, can simulate motions with remarkable similarity to experimental data. However, reflex-based controllers require for the entire set of parameters to be optimised in order to simulate different versions of the same motor behaviour (Song & Geyer, 2012, 2015). A recent reflex-based controller (Ramadan, Meischein, et al., 2022) addressed this issue by including an inverse model in the control architecture, indicating that the high dimensionality problem can be solved by including higher control centres. Moreover, neural controllers are typically task-specific, thus a combination of multiple controllers is needed to simulate different motor behaviours. As a case in point, Van der Kruk & Geijtenbeek (2023) developed a Sit-To-Walk model which integrated a controller dedicated to rising from a sitting position, and another dedicated to walking.

Physiological plausibility is the capability of a control architecture to represent actual structures of the nervous system. Controllers that incorporate central pattern generators (Taga et al., 1991; Ogihara & Yamazaki, 2001; Dzeladini et al., 2014; Di Russo et al., 2023; Severini & Munoz, 2024) can significantly reduce dimensionality through the feedforward control exerted by these structures. However, in opposition to reflexes, which are partially documented (Rossignol et al., 2006; Prochazka, 2010), CPGs are not completely understood in humans (Minassian et al., 2017).

Modularity and hierarchical control can offer new possibilities for handling these limitations. Modularity has been proposed as a basic biomechanical constraint, as the generation of stereotyped motor outputs is not the effect of individual muscles but necessitate coordination across multiple muscles (Ting et al., 2015). This coordination is supposedly organised in muscle synergies or motor primitives, that are functional units of motor control (Dominici et al., 2011). The combination of a limited number of synergies results in the generation of different motor behaviours (Bizzi & Cheung, 2013).

Here, we propose the Internal Model-based Modular Controller (IMMC) as a solution to both the dimensionality and plausibility problems. This novel architecture integrates modularity and hierarchy control to replicate multiple lower limb motions. The architecture aims to be flexible, significantly reducing the number of parameters to map motion, while the modules can independently implement physiological principles of motor control. The IMMC is based on four assumptions: i) motion can be mapped to a correct arrangement of synergies located in the spinal cord (Bizzi & Cheung, 2013); ii) some synergies have a reflexive nature (Ivanenko et al., 2006); iii) a task-specific network is the result of applying a specific pattern of excitatory and inhibitory synapses, here referred to as an internal model (IM), to a set of synergies (Levine et al., 2014); and iv) a hypothetical higher layer, corresponding to the mesencephalic locomotor region (MLR), selects IMs in parallel or sequentially to accomplish specific objectives (Le Ray et al., 2011).

This modular architecture (Figure 1A) establishes a hierarchised flow of control that begins when the MLR sends a controlling signal to activate a specific IM. IMs presented here are a simplified version of the structures proposed by Wolpert et al. (1998) and Wolpert & Kawato. (1998). Their role is to apply spatial and temporal constraints and regulate the inter-synaptic connections of a selected set of muscle synergies (Figure 1B). The resultant configurations of muscle synergies define task-oriented networks, enabling specific motor behaviours. These synergies follow sinusoidal activation functions characterizing discrete bell-shaped burst of activity(Figure 1C). The outcomes of the networks are integrated into motor pools, along with other simpler sensory loops, forming a premotor area (Figure 1B).

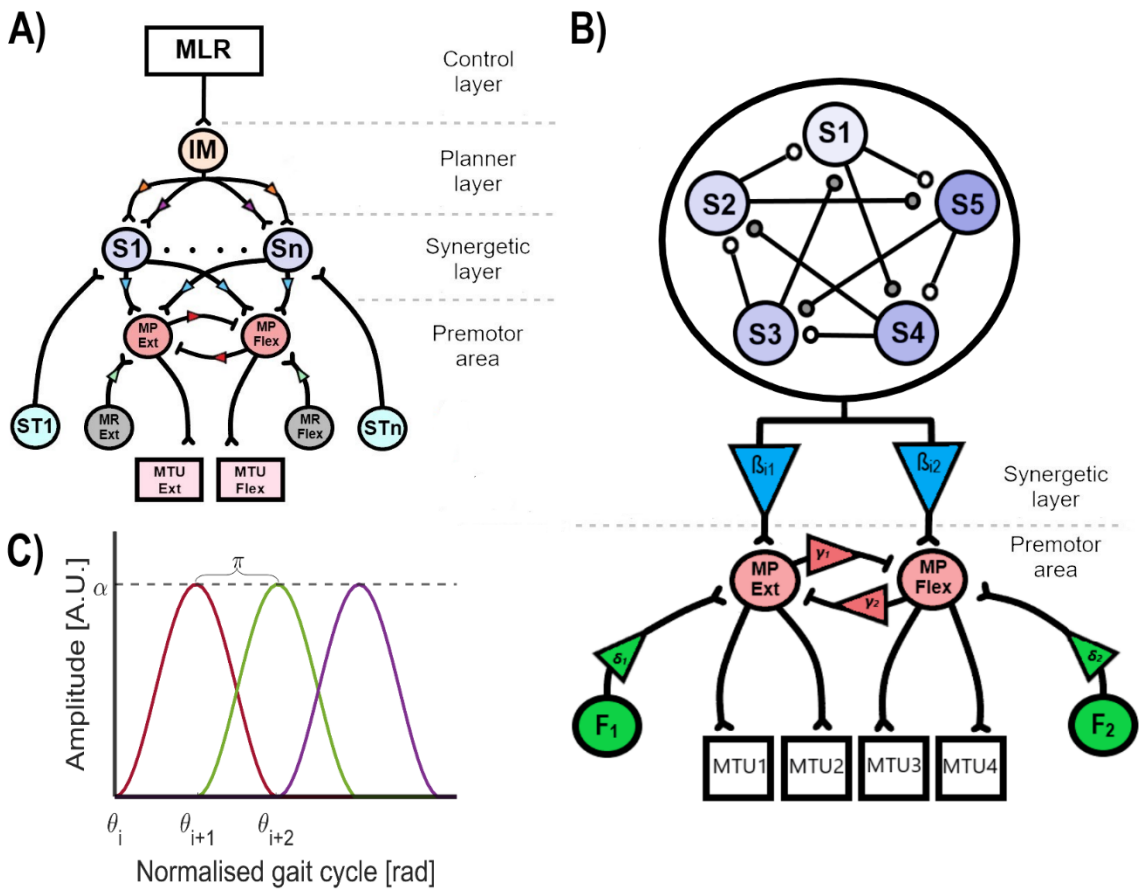

Figure 1. A) Scheme of IMMC, showing the hierarchy, from top to bottom, of MLR, IMs, synergies, premotor areas, and muscles. B) Organisation of five synergies in a network showing two different inhibitory synapses (white and grey circles) and its connection to the premotor area. C) Example of three synergies and their normalised distance of pi between them across the cycle of motion. Value α represent amplitude of the burst and θ their hypothetical trigger point.

Here the IMMC is tested in Stand-To-Walk (STW) transitions. The transition is represented by a change in the controlling signal from the MLR. Through the interplay of this signal with the IMs, the organisation of the network of the synergies shifts from a configuration related to standing to one related to walking (Figure 2).

The controller includes five synergies representing the principles of legged mechanics (Geyer & Herr, 2010): compliant-leg-behaviour, ankle-push-off, hip-unloading, swing, and leg-retraction (Figure 3). The IM dedicated to standing employs the compliant-leg-behaviour synergy to create a tonic output that drives quiet standing. When the MLR switches the controlling signal to 'walking', the standing-related network disappears. The walking IM, now activated, forms a new network, which also includes the compliant-leg-behaviour synergy, to create a rhythmogenesis that drives walking.

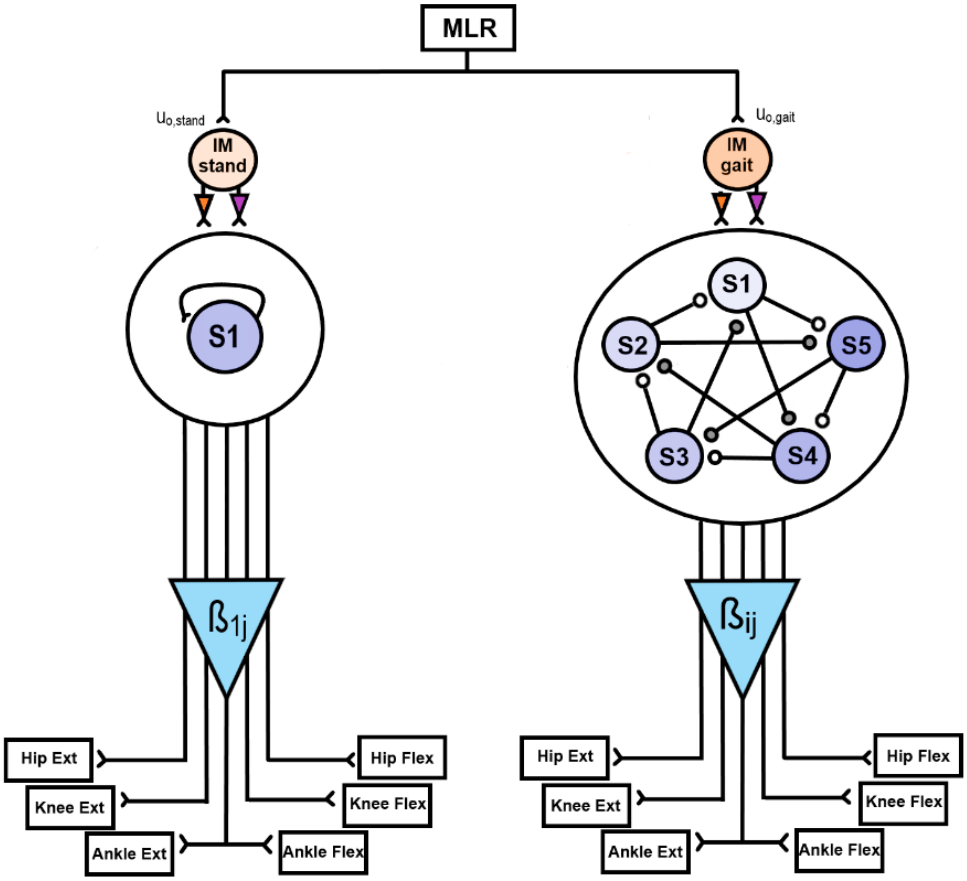

Figure 2. Flow of control of the IMMC from the MLR to the synergies. Two different networks are showed according to the controlling signal (u_o) of the MLR. Five different synergies are used to build these pathways.

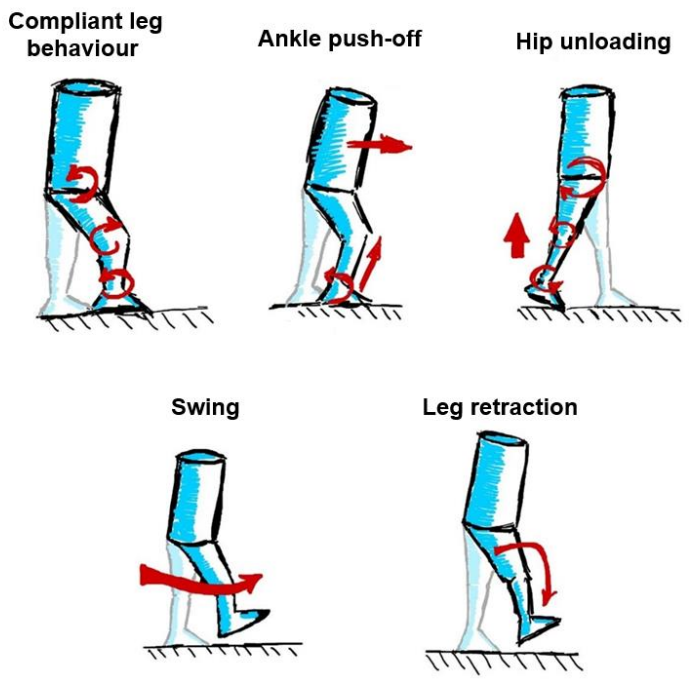

Figure 3. Principles of the legged mechanics. The figure presents the five principles of legged mechanics (Geyer & Herr, 2010), representative of the synergies implemented in the IMMC.

Results show a successful transition from standing to walking (1.3 ms^{-1}). The simulation results are consistent with human patterns. Also, the tuning of a unique signal achieves six speed transitions (0.8, 0.9, 1.2, 1.5, 1.6, and 1.8 ms^{-1}). The speed transitions did not require the complete set of parameters to be optimised. Instead, the walking-dedicated IM, already optimised for the 1.3 ms^{-1} scenario, regulates the rhythm of the system in response to the controlling signal.

We conclude that the IMMC has the potential to offer flexible solutions for various motor tasks in a unified architecture. This modular approach can integrate independent elements of feedforward and feedback control, representing different processes supported by neurophysiological evidence while maintaining low dimensionality.

Results

Stand-to-walk transition

The STW simulation lasts a maximum time (t) span of ten seconds. The simulation initiates with the controller performing the standing task, displaying an upright, quasi-static posture (Figure 4). After maintaining a stable standing behaviour for five seconds, the controller initiates gait and maintains it for the other five seconds. The MLR is the structure responsible for the task switching. At t = 5 s (t_{switch}), reflecting a conscious decision to start walking, the MLR changes the controlling signal, u_o, and deactivates the IM for standing (IM_{stand}) while activating the IM for gait (IM_{gait}). The consequent reorganization of the network of synergies results in the replacement of the tonic input related to standing with a walking-related rhythmogenesis. At a previous instant determined by t_{trans}, approximately t = 4.7 s, the MLR activates an additional IM, exclusively related to transition (IM_{trans}). This IM recruits a sixth synergy, called transition synergy, that helps to break the quiet standing and leans the torso forward. After a process of optimisation, IM_{gait} achieves a steady gait at a physiological value of 1.3 ms^{-1}.

The simulation produces the desired results. The controller maintains a stable quiet standing in the first half of the simulation, although slightly leaned backwards. At t_{trans}, the biomechanical model breaks the standing posture, and at t_{switch} it starts walking. At approximately t = 6.5 s, the gait reaches stability which is maintained until the end of the simulation. The average walking speed is around 1.3 ms^{-1}, while the average speed in the last step is 1.57 ms^{-1}. The average cost of transport is 3.7 $Jkg^{-1}m^{-1}$, close to the physiological energy expenditure in humans (Minetti et al., 2001; Umberger et al., 2003). The instantaneous anterior/posterior speed of the HAT, a unique segment in the biomechanical model that represent the head, arms, and torso, shows the transition in Figure 5.

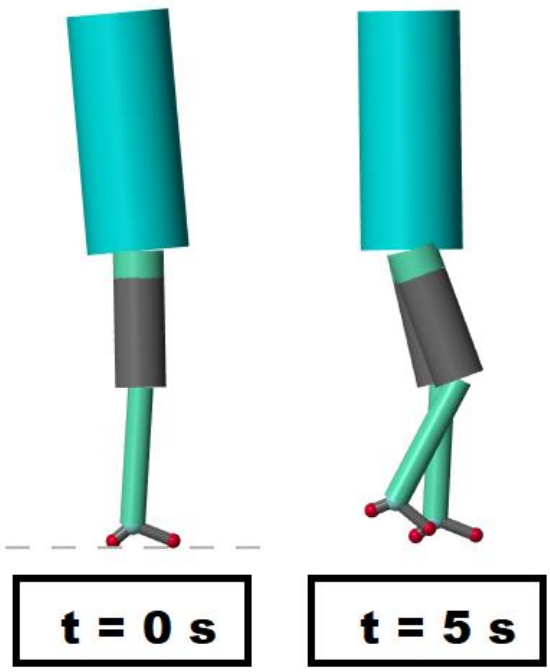

Figure 4. Right-side view of standing and walking in simulations.

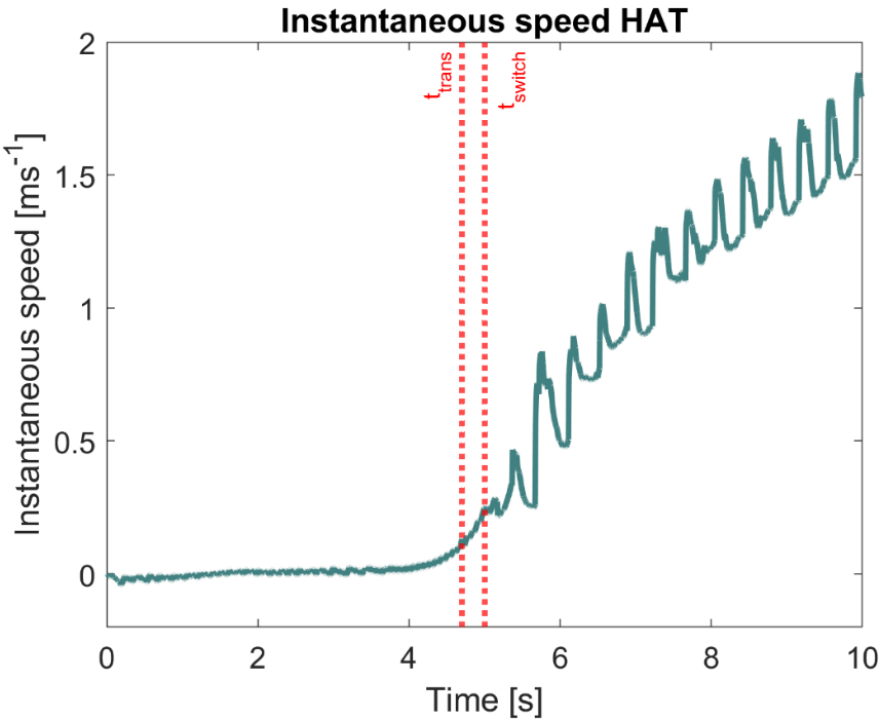

Figure 5. Instantaneous anterior/posterior speed of Head-Arms-Torso (HAT) shows the STW. The simulation corresponds to the original 1.3 ms^{-1} scenario.

Gait

Simulated data for the angular positions of hips, knees, and ankles during gait (5 s < t < 10 s) were compared to experimental data (Fukuchi et al., 2018). Figure 6A shows the comparison of the simulated trajectory of the joints over the gait cycle (averaged from the last three steps of the walking phase at 1.3 ms^{-1}) to the angular positions in humans. As first observation, the simulation foot-off occurs later, about 70 % of the gait cycle, with respect with what is usually experimentally observed according to Perry (2010), which is about 60 %. The simulated hip and knee angle are consistent with the experimental values but display a reduced flexion at the beginning and end of the stance phase.

The simulated ankle angles are slightly more plantarflexed than the experimental values for the first 50% of the gait cycle. For the second half of the cycle the simulated ankle displays more dorsiflexion. These observations are confirmed by a cross-correlation analysis (Table S1 in the Supplementary Material), with coefficient 'r' and lag 'Δ'. For the hips and knees, the coefficients are above 0.7 (r_{hip} = 0.90, Δ = 0 %; r_{knee} = 0.95, Δ = 1 %). However, for the ankles, the coefficients are r_{ankle} = 0.67, Δ = 6 %, caused by the commented plantarflexion/dorsiflexion and, generally, a longer stance phase.

In Figure 6B, muscle activation patterns throughout the gait cycle are shown, averaged across the final three steps the musculoskeletal model performs in the simulations. Muscle activation patterns are generally consistent with those expected in humans (Zajac, Neptune and Kautz, 2003) if we consider that the results are generally shifted to the right due to a prolonged stance phase. Rectus femoris is the exception, showing one of the two peaks that would be expected.

Figure 6C shows the weight-normalised ground reaction forces (GRFs), averaged across both legs during the final three steps of the simulation. The results match the typical pattern of contact force during walking (Fukuchi et al., 2018). The two peaks of the human GRF are noticeable. However, the first peak is bigger than expected. Moreover, we see two additional bumps, one at the beginning of the graph, just before the first peak, and other in the valley between the two peaks.

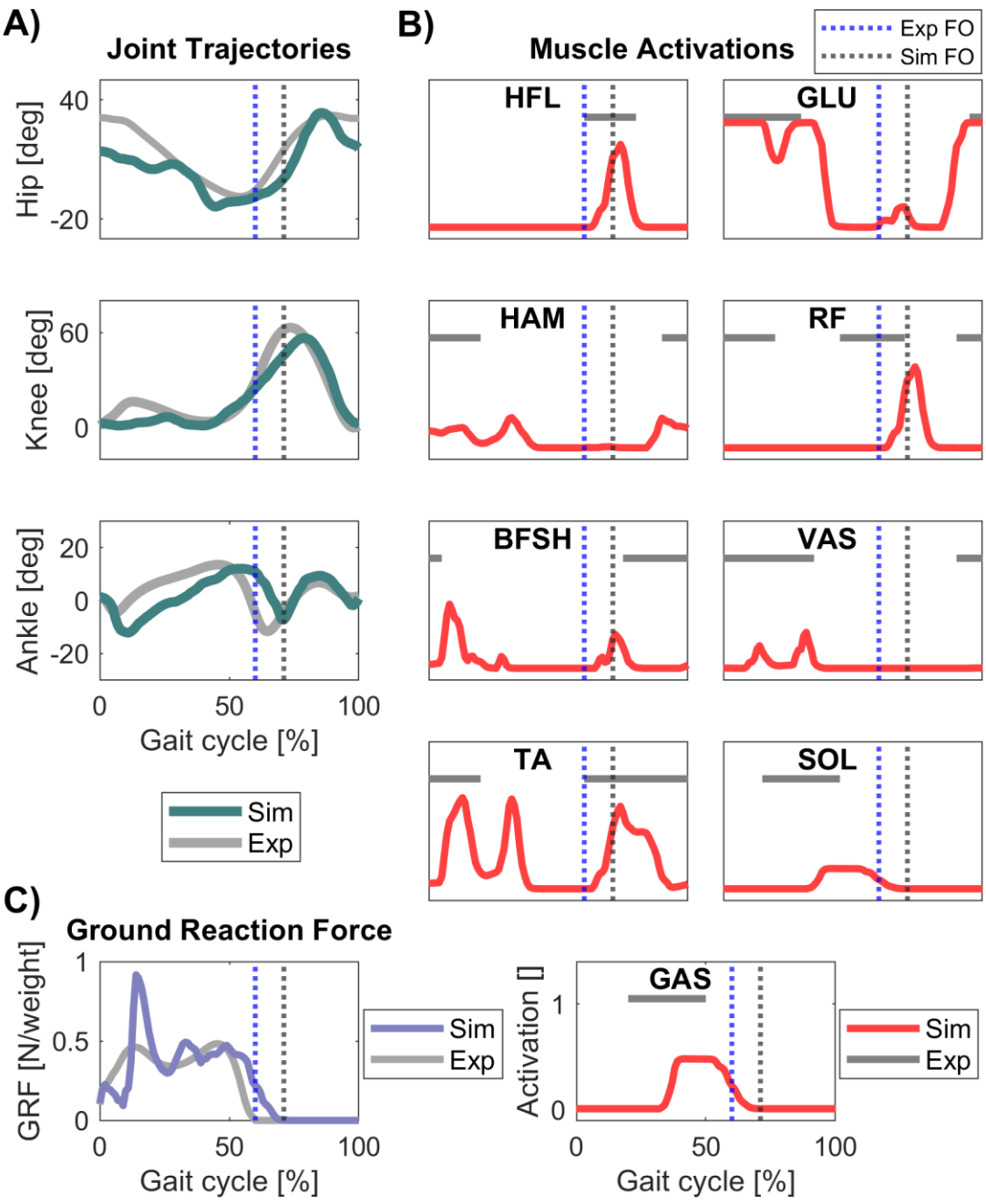

Figure 6. A) Experimental and simulated angular positions for hips, knees, and ankles at 1.3 ms^{-1}. Green: simulated data, grey: experimental data. B) Muscle activation patterns along the gait cycle at 1.3 ms^{-1}. Experimental data is given in the form of timing activation, interpreted from Zajac et al. (2003). C) GRF for the 1.3 ms^{-1} simulation across the gait cycle. Experimental GRF given by Fukuchi et al. (2018). Blue vertical dotted line: generic experimental foot-off (60 %) indicated by Perry (2010), black vertical dotted line: simulation foot-off (70 %).

Speed transition

This section describes simulations that demonstrate the ability of the MLR to modulate the speed of gait depending on the controlling signal. In the previous 1.3 ms^{-1} scenario, u_o had a constant value of 1. However, once the controller reaches stable gait at t = 6.5, u_o can be changed to values above or below 1 to activate variations in the parameters of IM_{gait}. These variations are responsible for the transition from 1.3 ms^{-1} to any of six other paces (0.8, 0.9, 1.2, 1.5, 1.6 and 1.8 ms^{-1}).

Figure 7A) shows the six speed transitions. At t = 6.5 s (t_{steady}), when the $u_{o,gait}$ varies, the instantaneous speed decreases or increases. In all cases, a new steady gait is achieved.

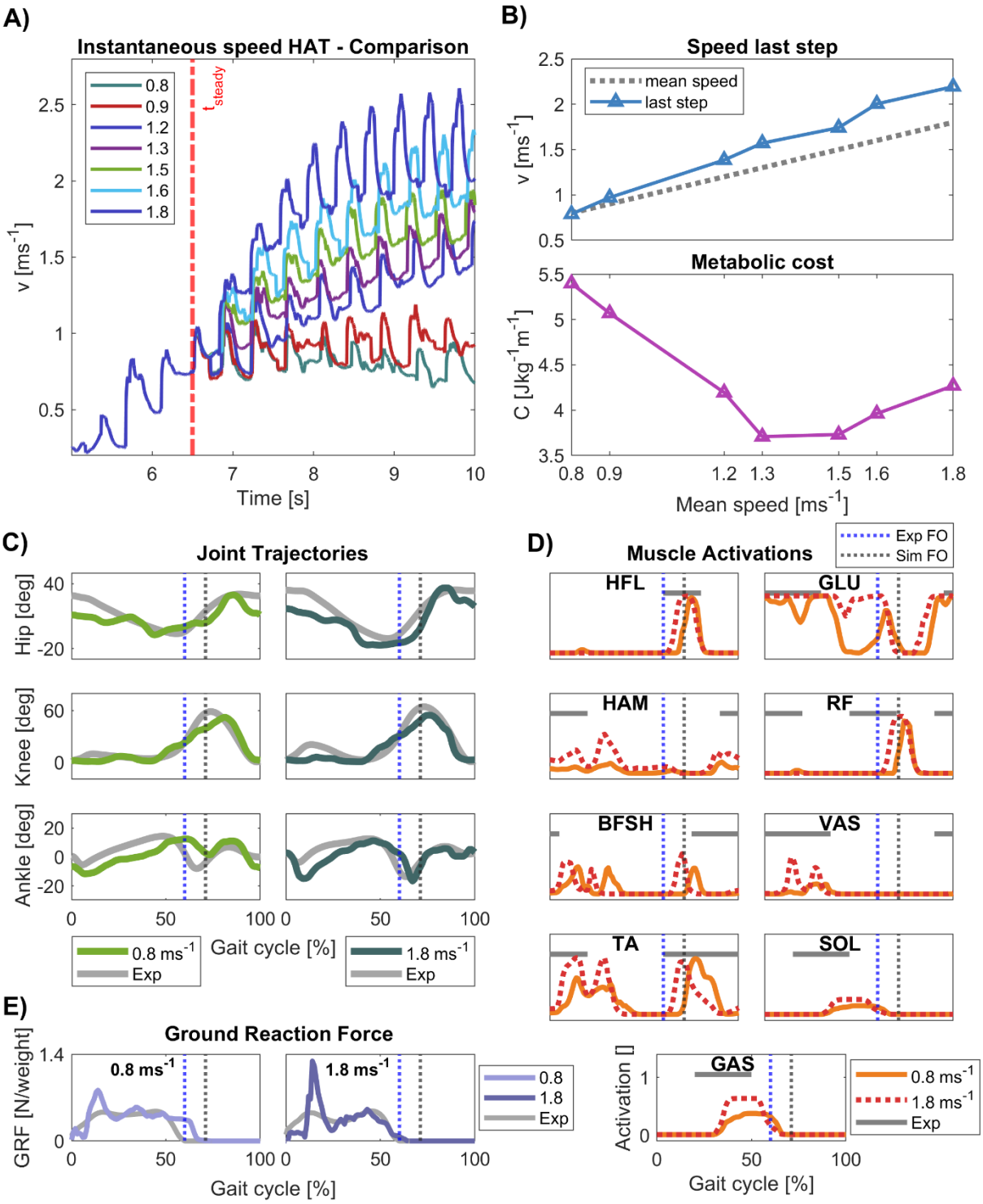

Figure 7. A) Instantaneous anterior/posterior speed of Head-Arms-Torso (HAT) during walking (from t = 5 s) at nine different speeds (0.8, 0.9, 1.2, 1.3, 1.5, 1.6, and 1.8 ms^{-1}). B) Last step (above) and metabolic cost (below) of all the simulated gait speeds. C) Experimental and simulated angular positions for the lower (0.8 ms^{-1}) and the upper (1.8 ms^{-1}) transitions. D) Muscle activation patterns for the left and right leg along the gait cycle for the lower and the upper transitions. Experimental data is given in the form of timing activation, interpreted from Zajac et al. (2003). E) GRF for left foot along the duration of walking for the lower (0.8 ms^{-1}) and the upper (1.8 ms^{-1}) transition, on the left and right, respectively. Experimental GRF given by Fukuchi et al. (2018). Blue vertical dotted line: generic experimental foot-off (60 %) indicated by Perry (2010), black vertical dotted line: simulation foot-off (70 %).

The relation between average speed, final speed (averaged during the last step), and metabolic cost is shown in Figure 7B. The first three transitions (0.8, 0.9 and 1.2 ms^{-1}) are consistent between the average and the final step speed, while the other simulations (1.3, 1.5, 1.6, and 1.8 ms^{-1}) increase the speed at the end of the simulation. The metabolic costs of transport are slightly higher than those values found for experimental results and other controllers (Song & Geyer, 2012).

The angular positions of the joints (average of the last three steps) in the lower (0.8 ms^{-1}) and upper (1.8 ms^{-1}) transitions are also consistent with experimental data of subjects walking at a slow and a fast pace (Fukuchi et al., 2018) (Figure 7C). The cross-correlation coefficients for hips and knees are presented in Table S1 (in the Supplementary Material). Simulation results are consistent with experimental data, except with the ankle trajectories for the 0.8 ms^{-1}, 0.9 ms^{-1} transitions. In these cases, as we observed in the case of 1.3 ms^{-1} simulation, the ankle angular positions are persistently plantarflexed in the first half of the gait cycle and dorsiflexed in the foot-off. The foot-off indicated with a vertical dotted line corresponds to the original simulation (1.3 ms^{-1}).

The muscle activation patterns (average of the last three steps) are consistent with the human patterns (Figure 7D). Again, the exception is the rectus femoris (Zajac, Neptune and Kautz, 2003).

GRF is similar to the sample of 1.3 ms^{-1} (Figure 7E) and to experimental samples (Zajac, Neptune and Kautz, 2003). However, the difference from the first and the second peak is increased for the sample of 1.8 ms^{-1} and attenuated for the sample of 0.8 ms^{-1}. Again, we can observe the two additional bumps before and between the peaks.

Discussion

Achievements of the STW application

The results show that the IMMC is successful in achieving the four objectives proposed for the STW transition in the Introduction. i) IMMC can complete a Stand-To-Walk transition in simulations when the MLR switches the controlling signal. ii) The controller effectively shares the compliant-leg-behaviour synergy between networks, showing a different role for standing and walking. iii) The controller can adjust to different speeds in response to a unique controlling signal. iv) The comparison of the simulation results with experimental data shows that the controller replicates human-like walking.

The IMMC surpasses the dimensionality limitations of current neural controllers and is designed to be physiologically plausible. The controller maps standing and gait with a unified architecture and the transition between the two tasks and within different gait speeds requires the adjustment of a unique signal. Reflex-based controllers, such as Geyer & Herr (2010) or Song & Geyer (2015), achieve gait with biomechanics close to human, but all the parameters must be optimised to achieve different motor outputs. Also, the IMMC does not require the combination of multiple controllers to achieve different tasks, like in the Sit-To-Walk controller of Van der Kruk & Geijtenbeek (2023), but rather the definition of task-specific IMs. The encapsulation of this information in IMs is flexible, as motion tasks can be changed while the rest of the system remains constant. It also simplifies the control dimensionality, as the activation of IMs are managed by a few controlling signals.

In comparison to CPG-based controllers, IMMC also offers plausible and efficient feedforward control. Taga et al. (1991), presented an CPG that could transition from walking to running by employing a unique signal. The controller was inspired in the proposal of Grillner (1975), where the unit generators are fed by other units, descending commands, and peripheric signals. However, the architecture of the generator was based on the continuous oscillator of Matsuoka (1985). In the IMMC, when triggered, the synergies display a bell-shaped burst of activity. Although the oscillators are a more physiological model, these discrete bursts are easier to characterise and more convenient, as they can be manipulated by changing a few characteristics. Additionally, the synergies and their organisation in networks capture the principles of legged mechanics while representing a plausible feedforward control.

A CPG-based controller presented by Jo & Massaquoi (2007) successfully replicated a STW transition, including gait speed modulation. However, unlike the IMMC, this implementation did not include full Hill-type muscle dynamics, CPGs did not activate biarticular muscles, and the control exerted by the synergies did not include standing. Also, the speed control was constrained to acceleration and decreasing the speed to lower values than the original default gait was not possible.

Simulation results

The kinematics and muscular activation resulting from the simulations are generally consistent with experimental data. We observed some inconsistencies in the excessive duration of the stance phase, delimited by the foot-off event, which occurs at the 70 % of the cycle instead of the 60 %. Other minor abnormalities are the ankle trajectories, or the muscular pattern of the rectus femoris.

The prolonged stance phase is caused by a slight delay in the activation of the plantarflexors, soleus and gastrocnemius. The activity of these muscles is related to the ankle push-off synergy, which is triggered when the centre of mass of the torso segment overtakes the heel of the stance leg. Thus, the unusual length of the stance phase is either due to an inadequate choice of trigger or is caused by torso taking longer than expected to advance the heel. We speculate that the second option is correct, as it correlates with the extension observed in the hip trajectory. This could be caused by an observed posterior lean of the torso during the standing task, which was not appropriately corrected by the transition synergy.

Although the hip and knee angle also show discrepancies when their trajectory is compared to experimental data, the related cross-correlation coefficients show they are generally consistent with the expected angular positions. The ankle trajectories display low correlation coefficients, particularly for the 0.8, 0.9, and 1.3 ms^{-1} simulations. Compared to experimental values, the simulation ankle angle is more plantarflexed during the first half of the gait cycle and more dorsiflexed around foot-off.

Abnormalities in the ankle trajectory are commonly observed in simulations obtained from neural controllers. For example, several controllers (Song & Geyer, 2015; Ramadan, Geyer, et al., 2022; Di Russo et al., 2023; Severini & Munoz, 2024) have similarly produced abnormal ankle angles. However, other controllers like the one presented by Geyer and Herr (2010) show ankle kinematics that fit experimental data better than the IMMC. Dzeladini et al. (2014) also had a better trajectory. One possible explanation for this is that, as indicated by Schumacher et al. (2023), abnormal trajectories for

the ankle depend on the selection of the musculoskeletal model. Moreover, the biomechanical model used here (Song & Geyer, 2015) is more simple and has less accurate ankle trajectories than the models presented by Schumacher et al. (2023). This suggests that the coupling between the controller and the biomechanical characteristics of the model affects the quality of the results.

The muscular on-off activation patterns are compared with the on-off intervals observed experimentally in unperturbed gait. As we saw before, some patterns are apparently delayed through the gait pattern because of the longer duration of the stance phase. The rectus femoris is the only muscle for which the observed differences cannot be explained by this shift, as this muscle has only one peak in simulated activation compared to two peaks in experimentally-observed activation. A possible explanation of the abnormal activation could be found in the motor pools. While the other two biarticular muscles, hamstrings and gastrocnemius, are fed by the same motor pool as the gluteus and the soleus, respectively, the rectus has dual motor pool input. That means that this muscle receives one input from the hip flexor and another from the knee extensor. The two motor pools cannot generate the typical activation profile of the rectus femoris but this is neither generated by them individually. Thus, we hypothesise that an unknown element of control could be responsible of activating the rectus femoris and other biarticular muscles.

The GRFs show the characteristic two-peak waveform of walking gait, with the first peak related to heel strike and the second peak related to push-off. The first peak is noticeably higher and lower for the 1.8 ms^{-1} and the 0.8 ms^{-1} simulations respectively, when compared to the 1.3 ms^{-1} simulation, as would be expected from physiological data. The two additional bumps we observed could be related to the prolonged stance phase. The second bump correlates with the activity of the plantarflexors before foot-off. The triggering of the ankle push-off synergy happens later than expected, resulting in an abnormal dynamic for the second peak. In the case of the first bump, it could be caused by a latency between the heel strike and the development of compliant force of the stance leg. This indicates that the compliant-leg-synergy could present problems with the excessive extension of the hip, taking longer to bring the centre of the mass of the torso forward.

Regarding the metabolic cost of transport, results are close to physiological values. For the 1.3 ms^{-1} simulation, the metabolic cost of transport is around 3.7 $Jkg^{-1}m^{-1}$ compared to the 3.5 $Jkg^{-1}m^{-1}$ displayed by humans (Umberger et al., 2003) and other simulation results (Song & Geyer, 2012).

Potential of the IMMC

The IMMC is the first attempt to present a new architecture that exhibits flexibility and neurophysiological plausibility, combined with internal models and hierarchised control. It is expected that the results of the simulations can be improved in future applications.

A logical next step for this work is to explore the dynamics of the synergies in the current implementation of the IMMC. Here, as in similar works (Di Russo et al., 2023; Severini & Munoz, 2024), synergies were modelled as bell-shaped bursts, although more physiological activation profiles could be devised. The equation of the synergies can be substituted by the oscillators of Matsuoka (1985) or another function that could reflect the dynamics of multiple sensory sources. Additionally, the role of some synergies

may be revised. For example, the shared synergy between both tasks, the compliant-leg-behaviour synergy, is here associated with quiet standing. However, Chvatal & Ting (2013) reported that this synergy could be related to the control of reactive standing. It is necessary to develop a more comprehensive vocabulary of synergies to replicate the whole range of quiet standing, reactive standing, and gait. Regardless of the role of the compliant-leg-behaviour synergy, the controller demonstrates that it is possible to generalise synergies across different behaviours (Allen et al., 2020).

Although this work is focused on the modularity of synergies, we propose to explore the use of additional sensory receptors and monosynaptic reflexes in future work. The IMMC may need the inclusion of more sensory triggers and modulators for a better alternance of synergies during the walking rhythmogenesis (McCrea & Rybak, 2008) or a more complete and accurate motor response at the premotor area (Rossignol et al., 2006). The implementation of these changes may allow the testing of the controller under different scenarios, including perturbations or noisy sensory inputs to test the robustness of the architecture.

With further development, the IMMC may achieve more ambitious objectives such as simulating Walk-To-Run, Walk-To-Stand, and Stand-To-Backward-Walk transitions. The inclusion of in-simulation update of the IMs could allow for testing of paradigms like the split-belt treadmill (Choi & Bastian, 2007) and the robot-induced perturbation paradigms (Severini et al., 2020) .

Overall, the IMMC applied to STW is successful considering the quality of the results and the suitability of the controller. Even though the current implementation may be considered simple, the IMMC displays the characteristics of modularity, hierarchical control, and stability. This provides the necessary flexibility to support an architecture that could eventually generalise control across lower limb motion.

Methods

Musculoskeletal model

The musculoskeletal model, including muscles, was implemented on Simulink following the proportions detailed in Song and Geyer (2015). The model represents a human body of 1.80 m height and 80 kg weight. It has seven segments representing HAT (head-arms-torso), thighs, shanks, and feet. The model has 6 degrees of freedom (DoF) as revolute joints connecting the segments (hips, knees, and ankles). Three additional DoFs were added to the model to define the movements of the biomechanical model with respect to the ground (longitudinal translation, anteroposterior translation, and pitch rotation). The muscle layer is composed of nine Hill-type muscle models: gluteus, hip flexors, hamstrings, rectus femoris, vastus, biceps femoris short head, gastrocnemius, soleus, and tibialis anterior.

Finally, the contact geometry consists of four contact spheres of 4 cm radius placed at the balls and heels of each foot. The whole musculoskeletal set is presented in Figure 4. The biomechanical model, and the rest of the IMMC, including the optimisation processes were implemented on Simulink/MATLAB R2022a.

Layers of the IMMC

The structure of the IMMC consists of four layers organised hierarchically. From higher to lower, these are the Control Layer, the Planner Layer, the Synergistic Layer, and the Premotor Area (Figure 1A).

Control layer

The Control Layer is the highest structure of the IMMC (Figure 1A). It consists of the mesencephalic locomotor region (MLR) that sends a limited number of control signals (u_o) to the rest of the system. The value of u_o depends on the internal model and the movement to control, specifically activating a unique internal model. For quiet standing, u_o is a discrete parameter that can be 0 or 1, indicating inactive or active, respectively. For gait, where the speed of walking is modulated, u_o could be 0 or a range of positive real values to control the rhythm of the system.

Planner layer

The Planner layer (Figure 1A) contains the internal models (IMs), which regulate the relationship between the synergies. The control exercised over the synergies is expressed by α gains, θ gains, and synapses. The α gains modulate the amplitude of the synergistic burst while the burst speed is regulated by the θ gains. The synapses establish excitatory or inhibitory connections between synergies. These three elements ensure that the output of the network of synergies matches the expected behaviour.

The Planning layer assures that the correct network of synergies is created according to the signalling from the superior layer, while blocking other configurations. The IMs are side-specific.

Synergistic layer

The Synergistic layer encompasses synergies (Figure 1A). Synergies are independent of each other until an IM organises them into a task-specific network. Each synergy represents a simple motor response based on a principle of legged mechanics (Geyer & Herr, 2010) and are independent in each leg.

The same synergy can be employed in different networks, pursuing diverse motor objectives. Modulations of one synergy can explain variations in the motor output, as observed in neurophysiological studies (d'Avella et al., 2003; Severini et al., 2020; Zych et al., 2021).

A synergy is characterised by a sensory event that triggers a burst:

$$S_i = \alpha(1 + cos(2\pi\eta\omega(u_o > 0) + \pi)(t - \Delta t_{Si}) \quad (1)$$

where S_i is the output of the i-th synergy, η is a sensory modulation of the burst, ω is a modulation generated by the next synergy, t is the simulation time, and Δt_{Si} accounts for any delay in the synergies.

The parameter η is defined as:

$$\eta = \frac{\lambda_{Si}}{F_{Si} + \lambda_{Si}} \quad (2)$$

where λ_{Si} is a specific gain for the sensory afferent F_{Si} that modulates the i-th synergy. F_{Si} can be different from the sensory afferent that triggers the synergy or be absent. The function of these

modulators consists of prolonging the activity of synergy if it is biomechanically necessary. If absent, then F_{Si} = 0, λ_{Si} = 1, η = 1.

The parameter ω is defined as:

$$\omega = \frac{\pi}{\theta_{i+1} - \theta_i} \tag{3}$$

where θ_i and θ_{i+1} are the θ gains for the current and the next synergy in the movement cycle, respectively. In the controller, each synergy is defined in a cycle that goes from 0 to 2π, whether it generates a rhythmogenesis or not. In the case where a single synergy is required for the organisation of a network like the standing behaviour and the transition to walk, θ_{i+1} is the θ gain of a virtual synergy that defines the frequency of the bursts.

The delays for the synergies are determined by the trigger and/or the sensory modulator. They can be short, medium, or long delays (5, 10, or 20 ms). The delays are assigned according to the related joint, HAT/hips, knees, and ankles, respectively. This implementation follows the scheme presented in Geyer et al. (2010; 2012).

Premotor layer

The last layer is the premotor area (Figure 1B). The basic components of this layer are the motor pools. These are hypothetical well-defined groups of motoneurons that integrate outputs from different sources and send an activation signal to the MTUs (Maegele et al., 2002; Romanes, 1964). Here, motor pools are organised in agonist/antagonist pairs for each joint and are side-specific.

Beside synergies, each motor pool integrates the output of monosynaptic reflexes. The monosynaptic reflexes are specific for a motor pool, and do not stimulate muscles in synergy. They are represented by linear functions:

$$\kappa_k = \delta_k F_k (t - \Delta t_{Fk}) \tag{4}$$

where κ_k is the k-th monosynaptic reflex for a motor pool, and δ_k is the synaptic weight of the k-th sensory afferent, F_k, to the motor pool. Again, Δt_{Fk}, determines the delay for the specific F_k as in equation 1.

The activation output of the j-th motor pool is defined as:

$$y_j = \sum_{i=1}^{n} \beta_{ij} S_i + \sum_{k=1}^{m} \kappa_k - \gamma y' \tag{5}$$

where β_{ij} is the synaptic weight between the i-th synergy and the j-th motor pool, n is the number of motor pools in the system, and m is the number of monosynaptic reflexes connecting to that motor pool. The input y' is an inhibitory modulation from the antagonist motor pool, which synaptic weight is represented by γ.

Each motor pool receives inputs from every synergy. As β_{ij} can take positive or negative values, this structure allows synergies to inhibit the activity of monosynaptic reflexes. However, γ and κ_k can be

directly modulated by the IMs. The scheme of the premotor area and its coupling with the synergies are presented in Figure 1A.

Muscles receive input from the motor pool to which they are anatomically related. The biarticular muscles gastrocnemius and hamstrings receive the same input as soleus and gluteus, respectively, as their patterns during the gait cycle are similar. However, the activation input is scaled by a factor, S_{SOL} and S_{GLU}. The biarticular rectus femoris is fed from the hip flexor motor pool and the extensor knee motor pool, with no scale factors, as its pattern presents similarities with vastus and hip flexors.

Application to standing

The specific application of the IMMC to standing consists of the controlling signal, $u_{o,stand}$, the IM_{stand}, and a unique synergy. The MLR applies $u_{o,stand} = 1$ at $t = 0$ s until $t_{switch} = 5$ s. The task is overseen by IM_{stand} that imposes the α and θ gains ($\alpha_{stand,1}$, $\theta_{stand,1}$, and $\theta_{stand,2}$) to the synergy.

The only synergy used by IM_{stand} represents the compliant leg behaviour (Geyer & Herr, 2010), which creates the standing network (Figure 2). An auto-excitatory synapse is established for the burst of the compliant-leg-behaviour synergy to display a tonic activation. This synergy establishes a dynamic to resist gravity, keeping the legs extended. The sensory trigger is the foot-ground contact of the leg to start stance (Ipsilateral leg load > 20 N). The synergy has a sensory modulator, the positive force of the vastus muscle (F_{S1} = VAS F+), that is closely related to the compliant leg behaviour. The motor pools receive the input from the compliant-leg-behaviour synergy according to equation 5, where the weights of synergies are grouped in $ß_{1j}$. The delay for this synergy is set to long (20 ms).

Three linear reflexes are implemented to achieve stability in hips, knees, and ankles. For the hips, the proprioception of hip joint will be responsible to maintain the correct position of HAT:

$$\kappa_{hip} = \begin{bmatrix} \phi_{hip} & \dot{\phi}_{hip} \end{bmatrix} \begin{bmatrix} \delta_{q,ext} & \delta_{q,flex} \\ \delta_{\omega,ext} & \delta_{\omega,flex} \end{bmatrix} (t - \Delta t_{\phi}) \tag{6}$$

where κ_{hip} is the magnitude of the reflex for hip pair, φ_{hip} is the angular position of the hip, $\dot{\varphi}_{hip}$ is the angular velocity of the hip, $\delta_{q,ext}$ and $\delta_{q,flex}$ are the synaptic weights of the angular position to the extensor and the flexor motor pools, and $\delta_{\omega,ext}$ and $\delta_{\omega,flex}$ are the synaptic weights of the angular velocity to the extensor and the flexor motor pools, respectively. Δt_{φ} is the delay for φ_{hip} and $\dot{\varphi}_{hip}$, set to short (5 ms).

For the knees, the extensor motor pool is inhibited by 'pain', a nociception that measures the knee joint extending beyond its soft limits:

$$\kappa_{knee} = \delta_{knee} P_{knee} (t - \Delta t_P) \tag{7}$$

where δ_{knee} is the synaptic weight for pain of the knee, P_{knee}. Δt_P is the delay for P_{knee}, set to medium (10 ms).

The afferent for the motor pools of the ankles, κ_{ankle}, is defined according to the relative contact force on the ball and the heel of the feet:

$$\kappa_{ankle} = [\delta_{ankle,ext} \quad \delta_{ankle,flex}] \frac{f_{ball}}{f_{ball} + f_{heel}} (t - \Delta t_f) \tag{8}$$

where f_{ball} and f_{heel} are the contact forces for the ball and the heel with the ground, and $\delta_{ankle,ext}$ and $\delta_{ankle,flex}$ are the synaptic weights for the extensor and flexor motor pool, respectively. This reflex is a measure of the CoP displacement that elicits a reactive coactivation of the ankle muscles. Δt_f is the delay for f_{ball} and f_{heel}, set to long (20 ms).

STW transition

The objective of the STW transition is breaking the standing dynamic based on a tonic output to create a new one for gait, which is based on a rhythmogenesis. The break of dynamics is achieved through the change of IM, and the introduction of a sixth synergy that will break stance and propel the body forward before walking. Like the standing dynamics, $u_{o,trans}$ is set to 0 or 1, which activates the transition synergy. This synergy is defined by the related IM, IM_{trans}, that has an similar composition to IM_{stand}.

At t_{switch} = 5 s, the MLR switches the controlling signal, $u_{o,stand}$ = 0, and $u_{o,gait}$ > 0, causing IM_{stand} to become inactive and IM_{gait} active. At that instant, the compliant-leg-behaviour changes the gains to $\alpha_{gait,1}$ and $\theta_{gait,1}$ and the walking rhythmogenesis is generated. At a pre-selected time before t_{trans} = 4.7 s, $u_{o,trans}$ becomes 1 to switch again to 0 at t_{switch}. t_{trans} is calculated during the optimisation process. This dynamic represents a volitional intention to initiate gait.

Application to gait

IM_{gait} activates all the five synergies, except the transition one, and presents five α and five θ gains. This interplay creates the network of synergies for gait. The five synergies represent the principles of legged mechanics (Geyer & Herr, 2010). Each of them has associated sensory triggers and modulators (Table 1), and are regulated by the gains of the IMs:

1. Compliant-leg-behaviour. This synergy is shared by both IMs. For standing, it keeps the legs extended and in quiet standing, and for gait, it resists gravity during heel strike, and confers double pendulum dynamics during the stance phase. The sensory trigger is the foot-ground contact of the leg (Ipsilateral leg load > 20 N). The synergy has as a sensory modulator the positive force of the vastus muscle (F_{S1} = VAS F+). The related delay is long-term (20 ms). The gains associated with this synergy are $\alpha_{stand,1}$, $\alpha_{gait,1}$, $\theta_{stand,1}$, $\theta_{stand,2}$, $\theta_{gait,1}$, λ_{S1}, and $ß_{1j}$.

2. Ankle push-off. The purpose of this synergy is the forward impulse of the body. It is triggered when the CoM is stable inside the base of support (COM_x > $heel_x$). The positive force of the soleus muscle (F_{S2} = SOL F+) acts as a sensory modulator. This synergy is only used in gait. The related delay is long-term (20 ms). The gains associated with this synergy are $\alpha_{gait,2}$, $\theta_{gait,2}$, λ_{S2}, and $ß_{2j}$.

3. Hip unloading. In late stance, this synergy assures that the stance leg unloads the weight of the body when the contralateral leg is ready for weight transfer. The sensory trigger is based on the contralateral leg load (Contralateral leg load > 20 N). No sensorial modulator is modelled for this synergy. This synergy is only used in gait. The related delay is short-term (5 ms). The gains associated with this synergy are $\alpha_{gait,3}$, $\theta_{gait,3}$, λ_{S3} = 1, $ß_{3j}$.

4. Swing. The objective of this synergy is the forward impulse of the swing leg. The activity is triggered when the ipsilateral leg is free of the weight of the body (Loadipsi < 20 N). No sensory modulator is modelled for this synergy. This synergy is only used in gait. The related delay is long-term (20 ms). The gains associated with this synergy are $\alpha_{gait,4}$, $\theta_{gait,4}$, λ_{S4} = 1, and $ß_{4j}$.

5. Leg retraction. This synergy assures the landing of the swing leg. The activity is triggered when the heel of the swing leg reached the CoM ($Heel_x > COM_x$). No sensory modulator is modelled for this synergy. This synergy is only used in gait. The related delay is short-term (5 ms). The gains associated with this synergy are $\alpha_{gait,5}$, $\theta_{gait,5}$, λ_{S5}, and $ß_{5j}$.

6. Transition. This is an ad hoc synergy to ease the transition by breaking quiet standing before t_{switch}. This synergy is not triggered by a sensorial event but by the activation of the control signal ($u_{o,trans} > 0$),. This synergy has a sensory modulator (F_{trans}) which is based on the forward leaning of the HAT. The related delay is short-term (5 ms). The gains associated with this synergy are $\alpha_{trans,1}$, $\theta_{trans,6}$, λ_{S6}, and $ß_{6j}$. The synergy is only recruited by IM_{trans}.

Table 1. List of synergies and their corresponding function along the gait cycle, their corresponding sensorial triggers and modulators, and the associated gains.

Synergy	Function	Trigger	Modulator (F_{Si})	Gains
1) Compliant leg behaviour	Resist gravitational pull / maintain quiet standing	Ipsilateral leg load > 20 N	Vastus positive force feedback	$\alpha_{stand,1}$, $\alpha_{gait,1}$, $\theta_{stand,1}$, $\theta_{stand,2}$, $\theta_{gait,1}$, λ_{s1}, $ß_{1j}$
2) Ankle push-off	Forward impulse of the body	$COM_x > heel_x$	Soleus positive force feedback	$\alpha_{gait,2}$, $\theta_{gait,2}$, λ_{s2}, $ß_{2j}$
3) Hip unloading	Weight transference	Contralateral leg load > 20 N	-	$\alpha_{gait,3}$, $\theta_{gait,3}$, $ß_{3j}$
4) Swing	Forward impulse of the swing leg	Ipsilateral leg load < 20 N	-	$\alpha_{gait,4}$, $\theta_{gait,4}$, $ß_{4j}$
5) Leg retraction	Swing leg landing	$Heel_x > COM_x$	-	$\alpha_{gait,5}$, $\theta_{gait,5}$, $ß_{5j}$
6) Transition	Ease the Stand-To-Walk transition	$u_{o,trans} > 0$	Θ_{HAT}	$\alpha_{trans,1}$, $\theta_{trans,6}$, λ_{s6}, $ß_{6j}$

For walking, two equivalent inhibitory synapses are established between synergies according to their relative positions (Figure 1B). A strong inhibitory synapse is established from one synergy to the synergy two positions behind ($S_{i+2} \rightarrow S_i$). That means that $S_i = 0$ if $S_{i+2} > 0$. This mechanism avoids a synergy being still active when it is not needed anymore. A second synapse is established as a phase coupling (Strogatz, 2000). Here, one synergy controls the rhythm of the previous synergy ($S_{i+1} \rightarrow S_i$). The phase coupling is defined as:

$$\Phi = -c \cdot sin(\phi_{i+1} + \phi_i + \pi) \tag{9}$$

where c is the strength of the coupling, manually tuned to 10, and φ_i and φ_{i+1} are the phases of two consecutive synergies. Equation 1 then becomes:

$$S_i = \alpha\big(1 + cos(2\pi\eta\omega(u_o > 0) + \pi + \Phi)\big) \tag{10}$$

An alternative formulation of equation 1 was devised for the first (compliant-leg-behaviour), the second (ankle-push-off), and the fifth (leg-retraction) synergies whose phase coupling was better explained by an amplitude factor:

$$S_i = \alpha(1 + cos(2\pi\eta\omega(u_o > 0) + \pi) - 10S_{i+1}) \tag{11}$$

Finally, the inhibitory disynaptic connection between the pair of antagonists, represented by the γ gains ($\gamma = \{\gamma_{hip}, \gamma_{knee}, \gamma_{ankle}\}$) are modified by IM_{gait}:

$$\gamma' = \gamma + g\big(u_{o,gait} > 0\big) \tag{12}$$

where $g = \{g_{hip}, g_{knee}, g_{ankle}\}$ are specific constants that modify the γ gains, and γ' are the transformed γ gains that are applied in equation 5. The scheme of gait is presented in Figure 2.

Also, equation 6 undergoes a gait-related modification to change the default hip angle:

$$\kappa_{hip} = \Big(\big(\phi_{hip} + \phi_{hip,o}(u_{o,gait} > 0)\big) \quad \dot{\phi}_{hip}\Big)\begin{pmatrix}\delta_{q,ext} & \delta_{q,flex}\\ \delta_{\omega,ext} & \delta_{\omega,flex}\end{pmatrix}(t - \Delta t_{\phi}) \tag{13}$$

where $\varphi_{hip,o}$ is the reference value for hip angular position.

Speed control

The transition from standing to walking also implies a speed transition from 0 ms^{-1} to the speed preferred by humans, 1.3 ms^{-1} which by default is maintained until the end of the simulation, at t = 10 s. However, other steady state gait speeds can be achieved by modulating the value of $u_{o,gait}$.

Changes of the controlling signal are applied once steady gait is achieved, around t = 6.5 s. Variations of the controlling signal are used to map the i-th α and θ values, the $\alpha_{gait,i}$ and $\theta_{gait,i}$ gains, to the new modified gains, $\alpha''_{gait,i}$ and $\theta''_{gait,i}$, establishing polynomial functions:

$$\alpha''_{gait,i} = \alpha_{gait,i} + \sum \alpha_{gait,n,i}\big(1 - u_{o,gait}\big)^n \tag{14}$$

$$\theta''_{gait,i} = \theta_{gait,i} + \sum \theta_{gait,n,i}\big(1 - u_{o,gait}\big)^n \tag{15}$$

where $\alpha_{gait,n,i}$ and $\theta_{gait,n,i}$ are the sets of modifying gains, n indicates the n-th order of the polynomial function, which was determined in the optimisation process to be four.

The control signal, $u_{o,gait}$, is equal to 1 for the basic speed of 1.3 ms^{-1}. Slower and faster gaits are represented by lower and higher values of $u_{o,gait}$. The new modifying gains are used consistently for each speed, guarantying that the system only varies the speed in response to changes in $u_{o,gait}$.

Additionally, the reference value for hip angular position from equation 13 is modified according to the value of $u_{o,gait}$:

$$\phi^*_{hip,o} = \phi_{hip,o} u_{o,gait} \left(u_{o,gait} > 0\right) \tag{16}$$

Algorithm of optimisation

The algorithm of optimisation is the Covariance Matrix Adaptation Evolution Strategy (CMA-ES) (Hansen, 2006). This algorithm is widely used for neuromuscular simulations because the cost function is evaluated independently in each iteration, making it relatively resilient to the inherent noise of biomechanical systems (Zhang et al., 2017). Standing, transition, and walking behaviours are optimised in a single process with three stages.

Balance cost function

The parameters of the standing neural pathway to optimise include the ß gains related to the compliant-leg-behaviour synergy, $ß_{1j}$, the δ gains of equations 6-8, the three γ gains of the motor pools, the biarticular scale factors, and the λ gain associated with the first synergy, λ_{S1}. In total, 19 parameters were optimised. The θ and α gains of the IM_{stand} were hand-tuned to achieve a fast activation of the first synergy. The $\alpha_{stand,1}$ gain was set to 0.5, and $\theta_{stand,1}$ and $\theta_{stand,2}$ were set to 0 and 0.25. The cost function for stance, J_{stand}, is:

$$J_{stand} = (t_{max} - t_{sim}) + E \tag{17}$$

where t_{max} is the maximum time of simulation set to 10 s, t_{sim} is the duration of the simulation in which the model does not fall, and E is the mass-specific energy consumption (Umberger et al., 2003). E (Wkg^{-1}) is defined as:

$$E = h_A + h_M + h_{SL} + w_{CE} \tag{18}$$

where h_A is the activation heat rate, h_M is the maintenance heat rate, h_{SL} is the shortening-lengthening heat rate, and w_{CE} is the mechanical work rate of the contractile elements of the muscles. E is calculated over the duration of the simulation. All the parameters were calculated as in Umberger et al. (2003).

J_{stand} tries to maximise time without falling while minimising energy consumption. The δ, γ and biarticular scale factors are included in this optimisation, because the general control flow of the system cannot be guaranteed without the correct tuning of these parameters and because stand is the initial state of the model, applying the same processes of the premotor area to every other motor behaviour.

The agonist/antagonist pair for the knee were forced to be positively fed by the synergies to facilitate a better reuse for gait (minimum 0.015).

Gait cost function

The parameters related to gait that need to be optimised are: the five $\alpha_{gait,i}$ gains and five $\theta_{gait,i}$ gains for the IM_{gait}, the $\theta_{trans,6}$ and $\theta_{trans,1}$ of IM_{trans}, the rest of the ß gains of the system ($ß_{ij} \backslash ß_{1j}$), t_{trans}, λ_{S2}, λ_{S6}, and the three g gains. In total, forty-eight parameters were optimised in this stage. The gain $\alpha_{trans,6}$ is set to 0.5. Before applying the CMA-ES algorithm, the parameters were hand-tuned to achieve three steps. The cost function for gait (J_{gait}) is defined as:

$$J_{gait} = (t_{max} - t_{sim}) + 10|v_{tgt} - v_{sim}| + P + C \quad (19)$$

where t_{max} is set to 10 s, giving 5 s each for stand and gait, v_{tgt} is the objective speed of the simulation (at this stage, 1.3 ms^{-1}, representing the self-selected speed gait observed in humans), v_{sim} is the average speed achieved during the simulation, P is pain (the sum of joint torques when soft limits are exceeded) and C is the metabolic cost of transport. C ($Jkg^{-1}m^{-1}$) is defined as:

$$C = \frac{E \sum m_m}{m_{body}\, v_{sim}} \quad (20)$$

where m_m is the mass for each muscle and m_{body} is the whole mass of the body (80 kg).

General flow of optimisation

IMMC requires a comprehensive optimisation process. This process involves three stages where the previously introduced cost functions are evaluated, and the parameters are updated.

In the first stage, the standing behaviour is optimised, meaning that only the parameters related to this behaviour are adjusted according to the cost function dedicated to balance. Standing behaviour is maintained throughout the ten-second simulation by setting the MLR to neither switch the controlling signal nor trigger the transition synergy. Once the mass-specific energy consumption (E) decreases below 2.5 Wkg^{-1}, the optimisation proceeds to the second stage.

In the second stage, the MLR is set to trigger the transition at t = 5 s, and both cost functions, balance and gait, are utilised. All 67 parameters of the controller are optimised in this stage. The parameters related to gait had previously been hand-tuned to replicate three steps. When the parameters are optimised to achieve gait for at least 3 seconds and reduce E below 3 Wkg^{-1}, the optimisation progresses to the third stage.

The final stage is characterised by the optimisation of the 48 parameters related to gait and the use of the corresponding cost function. This stage continues until the end of the optimisation process, with a maximum of 600 iterations. The CMA-ES algorithm was set to 5 parents and 40 offspring in each generation. Equation 20 shows the flow of control of the stages.

$$stage = \begin{cases} 1, \\ 2 \quad if stage = 1 \quad \& \quad E < 2.5, \\ 3 \quad if stage = 2 \quad \& \quad E < 3 \quad \& \quad t_{sim} < 8 \end{cases} \quad (21)$$

Speed transition optimisation

For the optimisation of speed transitions, we selected the parameters of a successful STW simulation. Once the simulation reaches a steady walking (t = 6.5 s), the $u_{o,gait}$ changes to values above or below the default value for 1.3 ms-1 ($u_{o,gait}$ = 1) for increasing or decreasing gait speed. For lowering the speed to 0.8, 0.9 and 1.2 ms^{-1} the values chosen were $u_{o,gait,down}$ = {1.6, 1.4, 1.2}, respectively. For increasing the speed to 1.5, 1.6, and 1.8 ms^{-1}, the values were $u_{o,gait,up}$ = {0.8, 0.6, 0.4}. Six new parameters were

introduced, five new θ gains and one α gain, that modify the original gains of IM_{gait}. The modifying equations are:

$$\alpha'_{gait,i} = \alpha_{gait,i} + \alpha_{gait,m,1}(1 - u_{o,gait}) \tag{22}$$

$$\theta'_{gait,i} = \theta_{gait,i} + \theta_{gait,m,i}(1 - u_{o,gait}) \tag{23}$$

where $\alpha_{gait,m,1}$ and $\theta_{gait,m,i}$ are the six modifying gains for the i-th original gain, with a dedicated set for each speed. $\alpha'_{gait,i}$ and $\theta'_{gait,i}$ are the resultant modified gains. The modifying gains are optimised by the CMA-ES algorithm with 8 parents and 16 offsprings, while the number of iterations is 300. The cost function (J_{trans}) is defined as:

$$J_{trans} = 35\left|v_{tgt} - v_{sim,last}\right| + C + \frac{AP}{3} \tag{24}$$

where v_{tgt} is the target speed, $v_{sim,last}$ is the speed of the centre of mass in the anteroposterior axis in the last gait cycle, and AP is the deviations of the angular positions of the joints at heel strike respect to their mean. As six sets of $\alpha_{gait,m,1}$ and $\theta_{gait,m,i}$ were calculated, a total of 36 gains were obtained.

After the optimisation, the new set of modifying gains, $\alpha_{gait,n,i}$ and $\theta_{gait,n,i}$, from equations 14 and 15, were found with a second optimisation process (J_{trans2}) where the differences between $\alpha'_{gait,i}$ and $\theta'_{gait,i}$, and $\alpha''_{gait,i}$ and $\theta''_{gait,i}$ were minimised:

$$J_{trans2} = \left|\alpha'_{gait,i} - \alpha''_{gait,i}\right| + \left|\theta'_{gait,i} - \theta''_{gait,i}\right| \tag{25}$$

For the optimisation of J_{trans2} the algorithm used was the Sequential Quadratic Programming (SQP) algorithm, and the minimum was found using a numerical method that solves constrained nonlinear multivariable optimisation problems. This optimisation is iterated until J_{trans2} lowers below $1e^{-3}$. The new set of $\alpha_{gait,n,i}$ and $\theta_{gait,n,i}$ gains is composed only by ten gains, discarding the previous 36 $\alpha_{gait,m,1}$ and $\theta_{gait,m,i}$ gains.

Funding statement

This work was funded by Science Foundation Ireland (grants #21/FFP-P/10228 and #12/RC/2289_P2).

References

Allen, J. L., Carey, H. D., Ting, L. H., & Sawers, A. (2020). Generalization of motor module recruitment across standing reactive balance and walking is associated with beam walking performance in young adults. *Gait & Posture*, *82*, 242–247.

Bizzi, E., & Cheung, V. C. (2013). The neural origin of muscle synergies. *Frontiers in Computational Neuroscience*, *7*, 51.

Choi, J. T., & Bastian, A. J. (2007). Adaptation reveals independent control networks for human walking. *Nature Neuroscience*, *10*(8), 1055–1062.

Chvatal, S. A., & Ting, L. H. (2013). Common muscle synergies for balance and walking. *Frontiers in Computational Neuroscience*, *7*, 48.

d'Avella, A., Saltiel, P., & Bizzi, E. (2003). Combinations of muscle synergies in the construction of a natural motor behavior. *Nature Neuroscience*, *6*(3), 300–308.

Di Russo, A., Stanev, D., Sabnis, A., Danner, S. M., Ausborn, J., Armand, S., & Ijspeert, A. (2023). Investigating the roles of reflexes and central pattern generators in the control and modulation of human locomotion using a physiologically plausible neuromechanical model. *bioRxiv*, 2023–01.

Dominici, N., Ivanenko, Y. P., Cappellini, G., d'Avella, A., Mondì, V., Cicchese, M., Fabiano, A., Silei, T., Di Paolo, A., & Giannini, C. (2011). Locomotor primitives in newborn babies and their development. *Science*, *334*(6058), 997–999.

Dzeladini, F., Van Den Kieboom, J., & Ijspeert, A. (2014). The contribution of a central pattern generator in a reflex-based neuromuscular model. *Frontiers in Human Neuroscience*, *8*, 371.

Fukuchi, C. A., Fukuchi, R. K., & Duarte, M. (2018). A public dataset of overground and treadmill walking kinematics and kinetics in healthy individuals. *PeerJ*, *6*, e4640.

Geyer, H., & Herr, H. (2010). A muscle-reflex model that encodes principles of legged mechanics produces human walking dynamics and muscle activities. *IEEE Transactions on Neural Systems and Rehabilitation Engineering*, *18*(3), 263–273.

Grillner, S. (1975). Locomotion in vertebrates: Central mechanisms and reflex interaction. *Physiological Reviews*, *55*(2), 247–304.

Hansen, N. (2006). The CMA evolution strategy: A comparing review. *Towards a New Evolutionary Computation: Advances in the Estimation of Distribution Algorithms*, 75–102.

Hicks, J. L., Uchida, T. K., Seth, A., Rajagopal, A., & Delp, S. L. (2015). Is my model good enough? Best practices for verification and validation of musculoskeletal models and simulations of movement. *Journal of Biomechanical Engineering*, *137*(2), 020905.

Ivanenko, Y. P., Poppele, R. E., & Lacquaniti, F. (2006). Motor control programs and walking. *The Neuroscientist*, *12*(4), 339–348.

Jacquelin Perry, M. (2010). Gait analysis: Normal and pathological function. *New Jersey: SLACK*.

Jo, S., & Massaquoi, S. G. (2007). A model of cerebrocerebello-spinomuscular interaction in the sagittal control of human walking. *Biological Cybernetics*, *96*(3), 279–307.

Le Ray, D., Juvin, L., Ryczko, D., & Dubuc, R. (2011). Supraspinal control of locomotion: The mesencephalic locomotor region. *Progress in Brain Research*, *188*, 51–70.

Levine, A. J., Hinckley, C. A., Hilde, K. L., Driscoll, S. P., Poon, T. H., Montgomery, J. M., & Pfaff, S. L. (2014). Identification of a cellular node for motor control pathways. *Nature Neuroscience*, *17*(4), 586–593.

Maegele, M., Müller, S., Wernig, A., Edgerton, V. R., & Harkema, S. (2002). Recruitment of spinal motor pools during voluntary movements versus stepping after human spinal cord injury. *Journal of Neurotrauma*, *19*(10), 1217–1229.

Matsuoka, K. (1985). Sustained oscillations generated by mutually inhibiting neurons with adaptation. *Biological Cybernetics*, *52*(6), 367–376.

McCrea, D. A., & Rybak, I. A. (2008). Organization of mammalian locomotor rhythm and pattern generation. *Brain Research Reviews*, *57*(1), 134–146.

Minassian, K., Hofstoetter, U. S., Dzeladini, F., Guertin, P. A., & Ijspeert, A. (2017). The human central pattern generator for locomotion: Does it exist and contribute to walking? *The Neuroscientist*, *23*(6), 649–663.

Minetti, A. E., Pinkerton, J., & Zamparo, P. (2001). From bipedalism to bicyclism: Evolution in energetics and biomechanics of historic bicycles. *Proceedings of the Royal Society of London. Series B: Biological Sciences*, *268*(1474), 1351–1360.

Muñoz, D., De Marchis, C., Gizzi, L., & Severini, G. (2022). Predictive simulation of sit-to-stand based on reflexive-controllers. *Plos One*, *17*(12), e0279300.

Ogihara, N., & Yamazaki, N. (2001). Generation of human bipedal locomotion by a bio-mimetic neuro-musculo-skeletal model. *Biological Cybernetics*, *84*(1), 1–11.

Prochazka, A. (2010). Proprioceptive feedback and movement regulation. *Comprehensive Physiology*, 89–127.

Ramadan, R., Geyer, H., Jeka, J., Schöner, G., & Reimann, H. (2022). A neuromuscular model of human locomotion combines spinal reflex circuits with voluntary movements. *Scientific Reports*, *12*(1), 8189.

Ramadan, R., Meischein, F., & Reimann, H. (2022). High-level motor planning allows flexible walking at different gait patterns in a neuromechanical model. *Frontiers in Bioengineering and Biotechnology*, *10*, 959357.

Romanes, G. (1964). The motor pools of the spinal cord. *Progress in Brain Research*, *11*, 93–119.

Rossignol, S., Dubuc, R., & Gossard, J.-P. (2006). Dynamic sensorimotor interactions in locomotion. *Physiological Reviews*, *86*(1), 89–154.

Schumacher, P., Geijtenbeek, T., Caggiano, V., Kumar, V., Schmitt, S., Martius, G., & Haeufle, D. F. (2023). Natural and robust walking using reinforcement learning without demonstrations in high-dimensional musculoskeletal models. *arXiv Preprint arXiv:2309.02976*.

Severini, G., Koenig, A., Adans-Dester, C., Cajigas, I., Cheung, V. C., & Bonato, P. (2020). Robot-driven locomotor perturbations reveal synergy-mediated, context-dependent feedforward and feedback mechanisms of adaptation. *Scientific Reports*, *10*(1), 5104.

Severini, G., & Munoz, D. (2024). A physiologically inspired hybrid CPG/Reflex controller for cycling simulations that generalizes to walking. *bioRxiv*, 2024–09.

Song, S., & Geyer, H. (2012). *Regulating speed and generating large speed transitions in a neuromuscular human walking model*. 511–516.

Song, S., & Geyer, H. (2015). A neural circuitry that emphasizes spinal feedback generates diverse behaviours of human locomotion. *The Journal of Physiology*, *593*(16), 3493–3511.

Strogatz, S. H. (2000). From Kuramoto to Crawford: Exploring the onset of synchronization in populations of coupled oscillators. *Physica D: Nonlinear Phenomena*, *143*(1–4), 1–20.

Taga, G., Yamaguchi, Y., & Shimizu, H. (1991). Self-organized control of bipedal locomotion by neural oscillators in unpredictable environment. *Biological Cybernetics*, *65*(3), 147–159.

Ting, L. H., Chiel, H. J., Trumbower, R. D., Allen, J. L., McKay, J. L., Hackney, M. E., & Kesar, T. M. (2015). Neuromechanical principles underlying movement modularity and their implications for rehabilitation. *Neuron*, *86*(1), 38–54.

Umberger, B. R., Gerritsen, K. G., & Martin, P. E. (2003). A model of human muscle energy expenditure. *Computer Methods in Biomechanics and Biomedical Engineering*, *6*(2), 99–111.

van der Kruk, E., & Geijtenbeek, T. (2023). A planar neuromuscular controller to simulate age-related adaptation strategies in the sit-to-walk movement. *bioRxiv*, 2023–11.

Wolpert, D. M., & Kawato, M. (1998). Multiple paired forward and inverse models for motor control. *Neural Networks*, *11*(7–8), 1317–1329.

Wolpert, D. M., Miall, R. C., & Kawato, M. (1998). Internal models in the cerebellum. *Trends in Cognitive Sciences*, *2*(9), 338–347.

Zhang, J., Fiers, P., Witte, K. A., Jackson, R. W., Poggensee, K. L., Atkeson, C. G., & Collins, S. H. (2017). Human-in-the-loop optimization of exoskeleton assistance during walking. *Science*, *356*(6344), 1280–1284.

Zych, M., Cannariato, A., Bonato, P., & Severini, G. (2021). Forward and backward walking share the same motor modules and locomotor adaptation strategies. *Heliyon*, *7*(8).

Supplementary Material

Table S1. Cross-correlation coefficients and lags of the simulation and the experimental (Fukuchi et al., 2018) joint angular positions.

Figure S1. A) Instantaneous anterior/posterior speed of Head-Arms-Torso (HAT) during walking (from t = 5 s) at nine different speeds (0.8, 0.9, 1.2, 1.3, 1.5, 1.6, and 1.8 ms-1). B) Last step (above) and metabolic cost (below) of all the simulated gait speeds. C) Experimental and simulated angular positions for the lower (0.8 ms-1) and the upper (1.8 ms-1) transitions. D) Muscle activation patterns for the left and right leg throughout the gait cycle for the lower and the upper transitions. Experimental data is given in the form of timing activation, interpreted from Zajac et al. (2003). E) GRF for left foot throughout the duration of walking for the lower (0.8 ms-1) and the upper (1.8 ms-1) transition, on the left and right, respectively. Dotted vertical lines indicate their respective vertical foot-off (1.3 ms-1).